APPLIED SCIENCES AND ENGINEERING

Active microgel particle swarms for intrabronchial targeted delivery

Hui Chen[1,2]†, Junhui Law[3,4]†, Yibin Wang[1,2], Ziheng Chen[1,2,5], Xingzhou Du[1,2], Kaiwen Fang[1,2], Zhe Wang[6]*, Feng Duan[7]*, Yu Sun[3,8,9]*, Jiangfan Yu[1,2]*

Intrabronchial delivery of therapeutic agents is critical to the treatment of respiratory diseases. Targeted delivery is demanded because of the off-target accumulation of drugs in normal lung tissues caused by inhalation and the limited motion dexterity of clinical bronchoscopes in tortuous bronchial trees. Herein, we developed microrobotic swarms consisting of magnetic hydrogel microparticles to achieve intrabronchial targeted delivery. Under programmed magnetic fields, the microgel particle swarms performed controllable locomotion and adaptative structure reconfiguration in tortuous and air-filled environments. The swarms were further integrated with imaging contrast agents for precise tracking under x-ray fluoroscopy and computed tomography imaging. Magnetic navigation of the swarms in an ex vivo lung phantom and in vivo delivery into deep branches of the bronchial trees were achieved. The on-demand reconfiguration of swarms for avoiding the microgel particles from entering nontarget bronchi and the precise delivery into tilted bronchi through climbing motion were validated.

INTRODUCTION

Pulmonary delivery of therapeutic agents has attracted extensive attention to treat lung diseases, such as lung cancer (*1*, *2*), cystic fibrosis (*3*, *4*), and pneumonia (*5*). Systemic administration, including oral route (*6*) and intravenous injection (*7*, *8*), delivers drugs and engineered nanoparticles to lesion sites through blood circulation, but off-target drug accumulation causes unmanageable toxicity (*9*–*11*). Intrabronchial delivery of therapeutic agents bypasses the first-pass metabolism in the liver (*12*, *13*). The inhalation method facilitates therapeutics in the lung (*13*, *14*), but inhaled agents are passively transported by airflow and unselectively distributed in the lung, negatively affecting healthy tissues (*8*). For local drug delivery, bronchoscopes are used to deploy drugs at a close distance to the target lesions through instillation (*15*, *16*) and direct injection (*17*). However, the motion dexterity of conventional bronchoscopes is limited for adapting to tortuous and narrow bronchi (*18*–*20*). Therefore, precise local deployment of drugs at target lesion sites in the lung needs to be achieved.

Active microrobotic swarms provide a promising approach to deliver therapeutic agents to hard-to-reach lesion sites in the human body (*21*–*26*). The swarms exhibit remote controllability (*27*–*29*), motion dexterity (*30*–*32*), and enhancement of medical imaging contrast (*33*–*35*) and have been demonstrated for the delivery of therapeutic agents (*36*, *37*). In particular, magnetic microrobotic swarms have been developed for targeted delivery in different physiological environments, including knees (*38*), eyes (*39*), and blood vessels (*40*–*42*). Driven by gradient fields, a swarm of magnetic microscaffolds was used to deliver stem cells to the position of cartilage defect in a rabbit knee (*38*). Magnetic swarms formed by slippery helical nanoswimmers were propelled in the vitreous humor of porcine eyeballs toward the retina (*39*). Under the guidance of x-ray fluoroscopy, particle swarms were shown to access the target region in rat livers (*41*) and porcine kidneys (*42*). However, for targeted delivery in the lung by active swarms, substantial challenges exist because of the nonfluidic environment, the existence of mucus layers, and the complex and unstructured bronchial tree.

Herein, we developed active microgel particle swarms for deep intrabronchial targeted delivery with medical imaging feedback (Fig. 1). Serving as composing agents of the swarms, the microgel particles were formed by hydrogel and magnetic microparticles coated with silica. Under external magnetic fields, the swarms performed controllable locomotion, reversible structure reconfiguration, and wall climbing in tortuous and air-filled environments. By integrating with imaging contrast agents, the swarms were tracked with medical imaging modalities. On-demand navigation of the swarms in an ex vivo porcine lung with mucus layers under x-ray fluoroscopy was demonstrated. In vivo delivery of the swarms into deep branches of bronchial trees was also achieved under computed tomography (CT) imaging, and the fluorescent dye encapsulated by the swarms was delivered and locally released to the target sites. This work provides a method to enable pulmonary targeted drug delivery and reveals the potential for precise treatment of lung diseases.

RESULTS

Features and characterization of the microgel particles

Microgel particles consisting of hydrogel and magnetic microparticles were used as the composing agents of the microrobotic swarms, and the hydrogel matrix encapsulated therapeutic agents. The contained magnetic microparticles enabled the remote maneuverability of microgel particles driven by magnetic fields. The microgel particles were observed by optical microscopy and scanning electron microscopy (SEM) (Fig. 2A). The average diameter of the prepared particles was ~650 μm (fig. S1). The elemental composition was characterized through energy-dispersive x-ray analysis, showing that the iron and silicon elements were contained in the microgel particles, which were

[1]School of Science and Engineering, Chinese University of Hong Kong, Shenzhen, China. [2]Shenzhen Institute of Artificial Intelligence and Robotics for Society, Shenzhen, China. [3]Department of Mechanical and Industrial Engineering, University of Toronto, Toronto, Canada. [4]Institute of Robotics and Intelligent Systems, Dalian University of Technology, Dalian, China. [5]School of Mechatronics Engineering and Automation, Shanghai University, Shanghai, China. [6]Department of Thoracic Surgery, National Cancer Center/National Clinical Research Center for Cancer/Cancer Hospital and Shenzhen Hospital, Chinese Academy of Medical Sciences and Peking Union Medical College, Shenzhen, China. [7]Department of Interventional Radiology, Chinese PLA General Hospital First Medical Center, Beijing, China. [8]Institute of Biomedical Engineering, University of Toronto, Toronto, Canada. [9]Robotics Institute, University of Toronto, Toronto, Canada.
*Corresponding author. Email: zhe.wang@live.cn (Z.W.); duanfeng@vip.sina.com (F.D.); yu.sun@utoronto.ca (Y.S.); yujiangfan@cuhk.edu.cn (J.Y.)
†These authors contributed equally to this work.

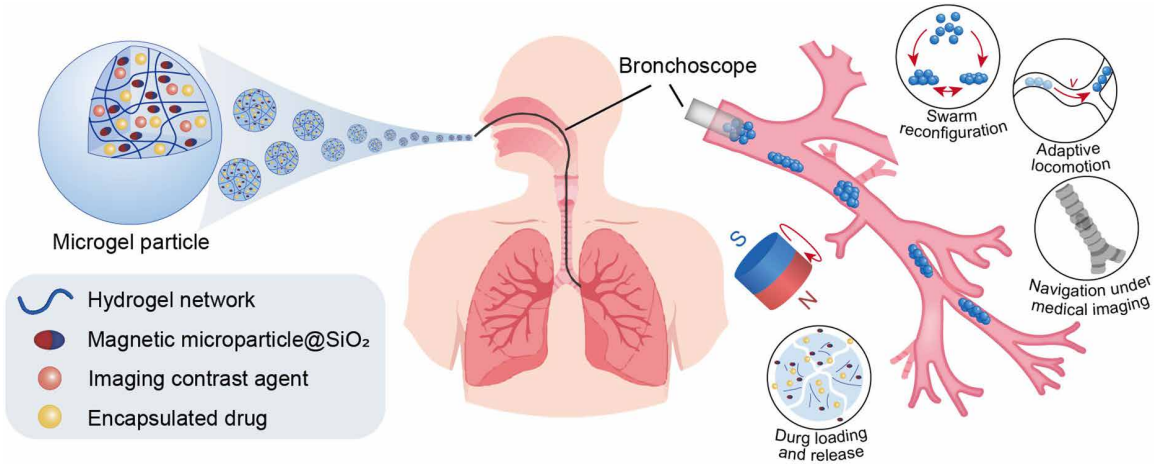

Fig. 1. Schematics of intrabronchial targeted delivery using microgel particle swarms. The microgel particles consist of hydrogel and magnetic microparticles coated with silica, allowing for the encapsulation of imaging contrast agents and drugs. A bronchoscope is used to deliver a swarm of microgel particles to the bronchus, followed by magnetic actuation to deeper branches. The swarms are capable of performing structure reconfiguration, adaptive locomotion in the tortuous bronchial tree, navigation under medical imaging, and release of encapsulated drugs.

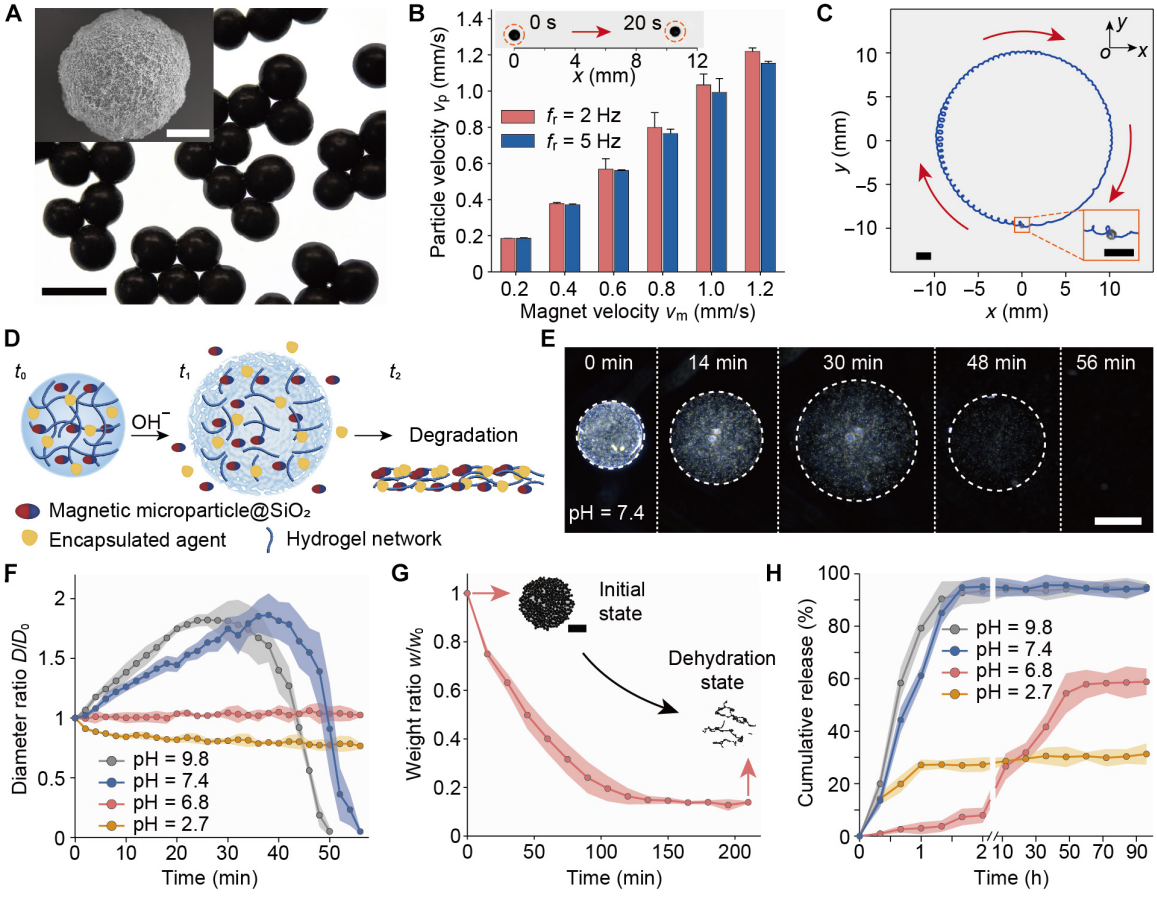

Fig. 2. Features and characterization of the microgel particles. (**A**) Optical image of the microgel particles. Scale bar, 1 mm. The inset image shows an SEM image of a microgel particle. Scale bar in the inset, 200 μm. (**B**) The relationship between the particle velocity v_p and the magnet velocity v_m with different rotating frequencies f_r. The inset image shows the translational locomotion of a microgel particle actuated by the magnet (v_m = 0.2 mm/s; f_r = 5 Hz). (**C**) Navigated locomotion of a microgel particle along a circular path. Scale bars, 2 mm. (**D**) Schematics of the pH-triggered swelling and degradation of a microgel particle to release encapsulated agents. (**E**) Swelling and degradation of a microgel particle in fluid with a pH of 7.4. Scale bar, 500 μm. (**F**) Relationship between the diameter ratio D/D_0 and time in fluids with different pH values. The initial diameter of the particles is D_0, and the particle diameter at each time point is D. (**G**) Relationship between the weight ratio w/w_0 and time. The initial weight of each particle is w_0, and w is the current particle weight with the fluid evaporation process. Scale bar in the inset, 5 mm. (**H**) Cumulative release of DOX from the microgel particles over time in the environment with pH values of 9.8, 7.4, 6.8, and 2.7. h, hours. The error bars and colored regions indicate the SD obtained from three trials.

major components of the magnetic microparticles coated with silica (fig. S2). The magnetic property of the microgel particles was evaluated by a magnetization curve, showing that the microgel particles were prepared with a remanence of 21.04 emu/g and a coercivity of 8.3 kOe (fig. S3). To actuate the microgel particles, a permanent magnet performing a rotational motion with a rotating frequency f_r and a translation motion with a velocity v_m was applied. The linear locomotion of a particle was demonstrated, and its velocity increased, from 0.2 to 1.2 mm/s, with the magnet velocity v_m (Fig. 2B). The navigated locomotion of the microgel particle along a circular path was also achieved (Fig. 2C and movie S1). It is noted that the rotational motion of the magnet was critical in the actuation of the particle, i.e., without rotational motion, the microgel particle was not propelled forward (fig. S4). The impacts of the working distance of the magnet on the particle locomotion were also investigated (fig. S5).

The microgel particles with porous network structures enable the loading of fluid for efficient delivery of therapeutic agents (*43*). The swelling and degradation of the particles can be triggered in alkaline environments to release the encapsulated agents (Fig. 2D). The changes of the microgel particle in the phosphate-buffered saline with a pH of 7.4 are shown as the dark-field images in Fig. 2E. The microgel particle swelled and then completely degraded within 56 min (Fig. 2E). To investigate the overall degradation behaviors of the microgel particles, the relationships between the diameter ratio D/D_0 and time in different conditions were quantified (Fig. 2F), and the particles in fluids with pH values of 9.8, 6.8, and 2.7 are shown in fig. S6. The initial diameter of the particles is D_0, and the particle diameter at each time point is D. The blue (pH = 7.4) and gray curves (pH = 9.8) increase from 1 to their peaks around 1.8 within 38 and 24 min, respectively, and then decrease rapidly to a value close to zero. The degradation of the outer area of the particles led to the reduction of hydrogel concentration, which made the outer area invisible. The decrease in the measured diameter ratio was thus caused. By contrast, minor influences were observed on the particles in the acidic environments with pH values of 6.8 and 2.7. In environments with a pH of 6.8, the diameter ratio D/D_0 of microgel particles was around 1 within 60 min (Fig. 2F). When the microgel particles were in environments with a pH of 2.7, the D/D_0 decreased from 1 to 0.77 within 50 min and then leveled out. The osmotic effect caused by the deprotonation of the carboxylic acid groups on the alginate could be the reason explaining the swelling and degradation features shown in Fig. 2 (E and F) (*43*). Swelling and degradation of microgel particle swarms were also studied (figs. S7 and S8 and Supplementary text S1). Furthermore, the ratio between the weight of the particles after evaporating the encapsulated fluid w and that of fully loaded particles w_0 was characterized (Fig. 2G). The ratio w/w_0 decreases with time and then levels out at around 0.18. Therefore, ~82% of the weight of a fully loaded particle could be the encapsulated drug, indicating the high loading capacity of the particles. Moreover, the release of doxorubicin (DOX) from the microgel particles was investigated, which is a water-soluble model drug and commonly used for the treatment of lung cancer and lung metastasis (*44*–*46*). The cumulative released amount of DOX in environments with pH values of 9.8 and 7.4 increased rapidly to 90% within 80 and 100 min, respectively (Fig. 2H). Afterward, the releasing rates were reduced. Under the condition with a pH of 6.8, the released amount of DOX increased to about 58% within 60 hours, followed by a reduced releasing rate. In an acidic environment with a pH of 2.7, the released amount of DOX increased to 28% within 60 min, and then the releasing rate was decreased. The rapid releasing in alkaline environments was caused by the swelling and degradation of microgel particles. The results at pH 6.8 demonstrated the sustained release capability of swarms. The releasing rate of DOX at pH 2.7 was faster than that at pH 6.8 during the first 60 min and became slower than that at pH 6.8 after 60 min. These results could be caused by the size change of microgel particles. The size of microgel particles at pH 6.8 was almost not changed, while the microgel particles became condensed with a reduced size at pH 2.7 (Fig. 2F). In this case, during the first 60 min, the contained DOX was diffused passively from the microgel particles at pH 6.8, while it was actively squeezed out from the particles at pH 2.7. After 60 min, the condensed microgel particles constrained the contained DOX tightly at pH 2.7, resulting in a slower releasing rate compared to that at pH 6.8. Overall, these two releasing modes of the microgel particles, i.e., rapid and sustained release, allow on-demand drug releasing based on actual needs. The release of nintedanib from microgel particles was also investigated (fig. S9 and Supplementary text S2). Besides, cells could be encapsulated and released by the particles (fig. S10).

Controlled locomotion of the microgel particle swarms

By applying rotating magnetic fields using the permanent magnet, the microrobotic swarm was formed through gathering of the microgel particles (Fig. 3, A and B, and movie S2). Initially, the microgel particles were spread on the substrate, and after applying the rotating magnetic field with a frequency of 5 Hz, the particles moved toward each other, relying on time-varying magnetic dipolar interactions and attractive interparticle capillary forces (0 to 2 s). The microgel particle swarm was last formed at 6 s. The entire swarm generation process was performed in air. The detailed generation mechanism is explained in Supplementary text S3 and fig. S11.

The assembled planar swarm was propelled as an entity to move forward actuated by the external rotating magnet, as shown in Fig. 3C. When the rotating magnet was translated from the start to the target along a straight path with different velocities (i.e., 1 to 5 mm/s), the swarms reached the target with different trajectories (Fig. 3D). When the magnet velocity was larger than 2 mm/s, the swarms had curved paths. This phenomenon can be resulted from that, when the particles are far from the magnet center, the local magnetic field causes a pitch angle to the swarms, inducing the swarms to move with a curved trajectory (fig. S12). In the subsequent experiments, the magnet velocity v_m was thus limited lower than 2 mm/s to guarantee the precise motion actuation of the microgel particle swarms. Within this range, the swarm velocity increases linearly with the magnet velocity (Fig. 3E). The relationship between the swarm velocity and the working distance of the magnet was also investigated (fig. S13). The magnetic field gradient and gradient forces applied on swarms were quantified (fig. S14 and Supplementary text S4).

Furthermore, the microgel particle swarms were navigated in different environments to validate their adaptability and motion dexterity, as shown in Fig. 3 (F to H) and movie S2. The swarms climbed along tilted slopes with angles of 20° and 50° (Fig. 3F). The climbing velocity of the swarms decreases from 0.2 to 0.13 mm/s with an increase in the slope angle from 10° to 50° (v_m = 0.2 mm/s) (fig. S15). Swarm locomotion on descending slope surfaces was also realized (fig. S16 and Supplementary text S5). The microgel particle swarm could move on a wavy surface while maintaining its integrity through the particle-particle dipolar interactions and the interparticle capillary interactions (Fig. 3G). Moreover, a tube with a hole at

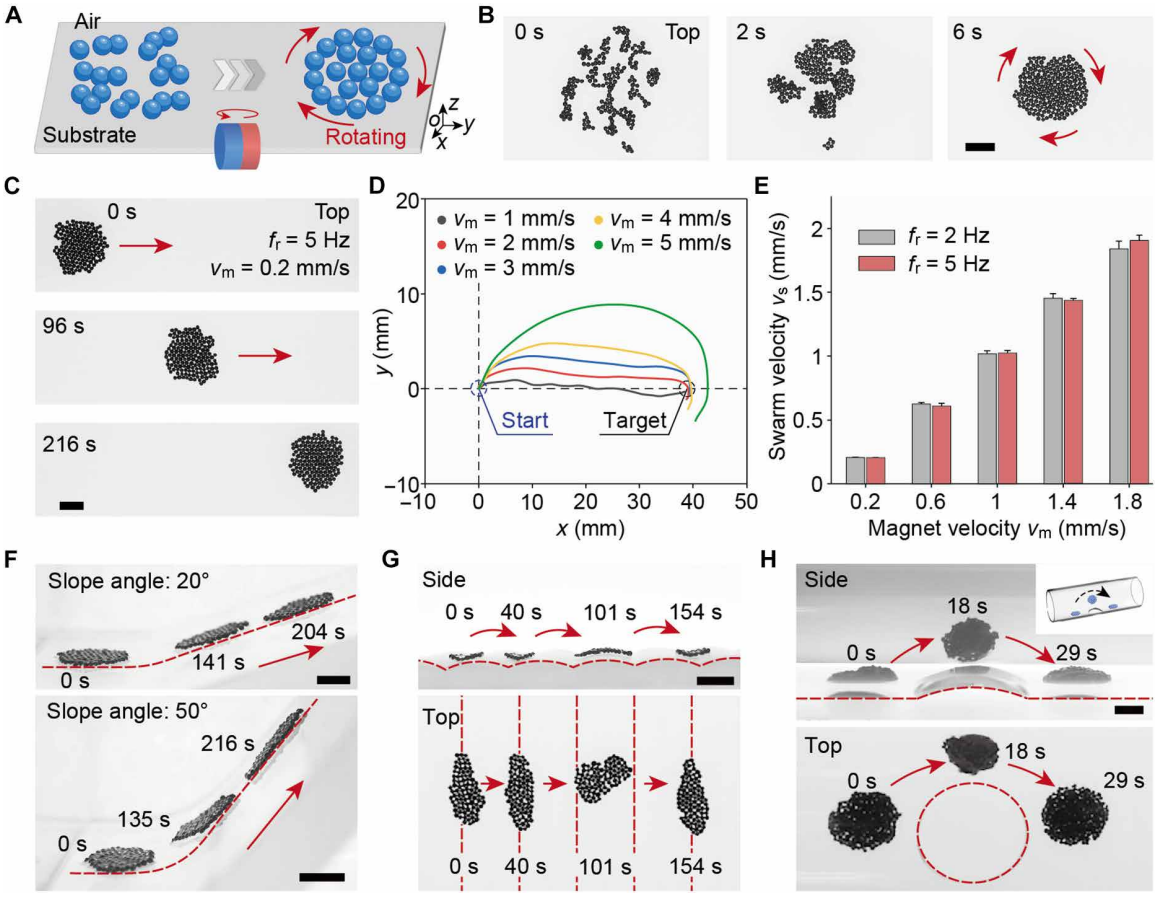

Fig. 3. Generation and navigated locomotion of the microgel particle swarms. (**A**) Schematics of the microgel particle swarm formation actuated by rotating magnetic fields. (**B**) Formation of the microgel particle swarms with a planar structure. (**C**) Forward locomotion of a planar swarm. (**D**) Trajectories of planar swarms actuated by the magnet with different velocities v_m. (**E**) Relationship between the swarm velocity v_s and magnet velocity v_m with different rotating frequencies f_r. (**F**) Climbing motion of the swarms on slopes with 20° and 50° tilted angles. (**G**) Swarm locomotion on a wavy surface. The red dashed lines in the top view highlight the waves between them. Each wave has a height of 0.75 mm and a width of 8 mm. (**H**) Wall climbing of the swarm in a tube to avoid the hole at the bottom. The error bars indicate the SD obtained from three trials. Scale bars, 5 mm.

the bottom, sharing similarity with the environments in bronchi, was applied, and the swarm was capable of climbing along the side wall to avoid from entering the hole (Fig. 3H).

Adaptive reconfiguration of the microgel particle swarms

The microgel particle swarms can actively respond to external magnetic fields to perform structure reconfiguration, and the schematics are shown in Fig. 4A. Actuated by the magnet performing oscillating motion with an oscillating angle α_0 and an oscillating frequency f_o, the swarm reconfigured from the planar structure to a pillar-like structure in air, and the experimental results are shown (Fig. 4B and movie S3). By applying the oscillating magnetic field (α_0 = 100°; f_o = 1 Hz), the particles in the planar swarm were vertically assembled into multiple three-dimensional (3D) clusters at 8 s (red dashed lines in the top view). The clusters then oscillated with the field, grew by attracting surrounding particles, merged with each other, and last, generated a pillar-like microgel particle swarm. The detailed reconfiguration mechanism is explained in Supplementary text S6 and fig. S17. Furthermore, the structure reconfiguration process was numerically simulated (Fig. 4C, Supplementary text S7, and fig. S18). The simulation results matched well with the experimental results and revealed that the dipolar interactions among the particles were critical for the structure reconfiguration of the swarms. By applying upward magnetic gradient force, the pillar-like swarm was transported vertically to the roof (fig. S19). Relying on the vertical lifting and the adaptive reconfiguration capability, the swarm was navigated in a confined 3D environment with a wall (Fig. 4D and movie S3). The pillar-like swarm was first lifted to the roof (0 to 10 s). By changing the direction and rotating frequency of the magnet (f_r = 5 Hz), the pillar-like swarm was subsequently spread to the planar state at the roof (104 s). The swarm was then navigated at the roof to pass through a narrow space limited by the wall (149 s). The swarm was reconfigured back into the pillar-like structure (227 s) to reduce the experienced capillary force and last landed on the substrate.

By tuning the field oscillating angle, the coverage area and height of the microgel particle swarms were adjusted (Fig. 4E). When the oscillating angle increased, the coverage area decreased, and the height of the swarms increased. The change of the coverage area and height of the swarms with the field oscillating angle was quantified (Fig. 4F and fig. S20). The swarm coverage area gradually decreases from about 100 to 30 mm^2, the swarm height increases from 1 to 6 mm

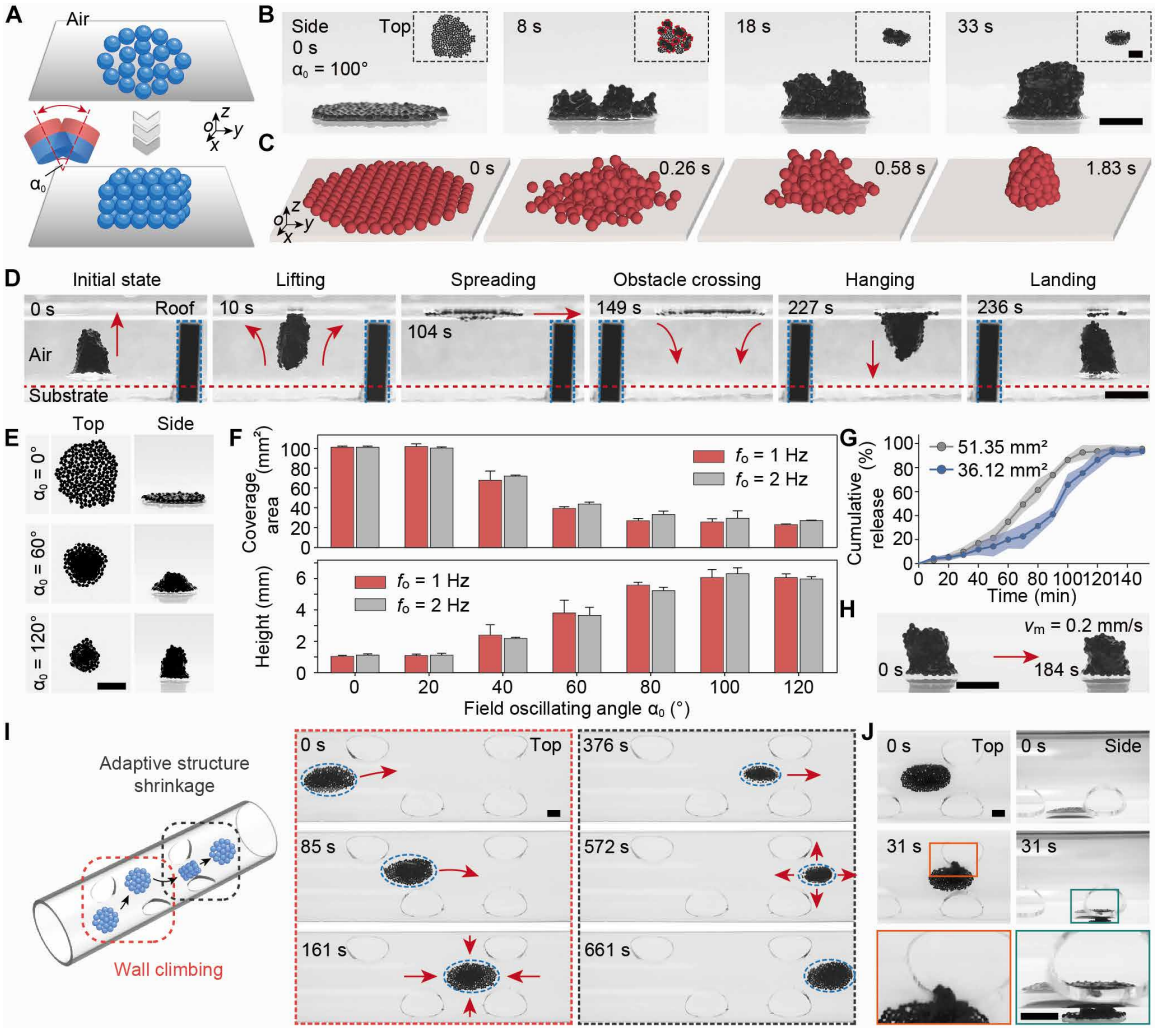

Fig. 4. Adaptive structure reconfiguration and locomotion of the microgel particle swarms. (**A**) Schematics of the swarm reconfiguration actuated by oscillating magnetic fields. The field oscillating angle is α_0. (**B**) Experimental results of the structure reconfiguration of the swarm. The regions highlighted by red dashed lines indicate the clusters. (**C**) Simulation of swarm reconfiguration. (**D**) Adaptive targeted locomotion of the swarm in an unstructured environment. (**E**) Experimental results of swarm coverage area actuated by fields with different oscillating angles α_0. (**F**) Quantitative change in the swarm coverage area and height with field oscillating angles α_0 when the oscillating frequencies f_o are 1 and 2 Hz. (**G**) Cumulative release of DOX from microgel particle swarms with different coverage areas over time. (**H**) Translational locomotion of a pillar-like swarm. (**I**) Schematics and experimental results of wall climbing (red dashed rectangle) and adaptive structure shrinkage (gray dashed rectangle) of a swarm in a tube with holes. (**J**) Particle loss of the swarm when moving along the narrow path in (I) without structure shrinkage. The error bars indicate the SD obtained from three trials. Scale bars, 5 mm.

when the field oscillating angle increases from 0° to 80°, and then both levels out. The working distance of the magnet also plays an important role in the reconfiguration of the swarms (fig. S21). The locomotion and reconfiguration of microgel particle swarms in a layer of mucus were also demonstrated (fig. S22 and Supplementary text S8). Furthermore, the influences of swarm structure on DOX release were studied, as shown in Fig. 4G. Swarm I was generated with a coverage area of 51.35 mm^2, and its surface area was estimated to be 152.50 mm^2 by approximating the swarm as a circular truncated cone (fig. S23), and swarm II was generated with a coverage area of 36.12 mm^2 and an estimated surface area of 111.43 mm^2. For swarm I with the coverage area of 51.35 mm^2, the cumulative released amount of DOX increased to 35% at 60 min, increased to 74% at 90 min, and leveled out at 95% within 110 min (Fig. 4G). The release rate was then reduced. In contrast, swarm II with the coverage area of 36.12 mm^2 exhibited a slower release rate, with 20% of DOX released at 60 min and 41% at 90 min (Fig. 4G). The cumulative released amount of DOX leveled out at 95% within 130 min. After a 3D swarm was formed, the swelling, degradation, and releasing of drugs occurred from the outer particles and gradually progressed toward the core part. Therefore, the swarm with a larger surface area could exhibit a higher drug release rate.

The capability of performing navigated locomotion was maintained when the swarm was at the pillar-like state (Fig. 4H), which had reduced coverage area for passing through narrow spaces. By switching the actuation mode, the swarm was navigated in a tube with holes (Fig. 4I and movie S3). The swarm first climbed around the wall and avoided the first two holes (0 to 161 s). Subsequently, the swarm reconfigured into the pillar-like structure to reduce the coverage area (376 s) and thus successfully adapted to the narrowed

path (376 to 572 s). After entering the free space, the swarm was reconfigured reversibly to the original structure (661 s). During the locomotion process, the integrity of the swarm was well maintained, and all the particles were delivered to the target. The control group without structure shrinkage was presented for comparison, and in this case, the particle loss was notable when passing through the narrow path at 31 s (Fig. 4J).

Swarm actuation and delivery in vitro and ex vivo

A bronchial tree is an air-filled and multibranched 3D structure. The schematics of the actuation and delivery of the microgel particle swarms into a tilted branch are shown (Fig. 5A). The in vitro validation was realized in a phantom of human bronchial tree. In the secondary bronchus, the swarm reached the upper surface by the direct lifting motion and the climbing motion around the inner surface of the bronchus wall (Fig. 5B

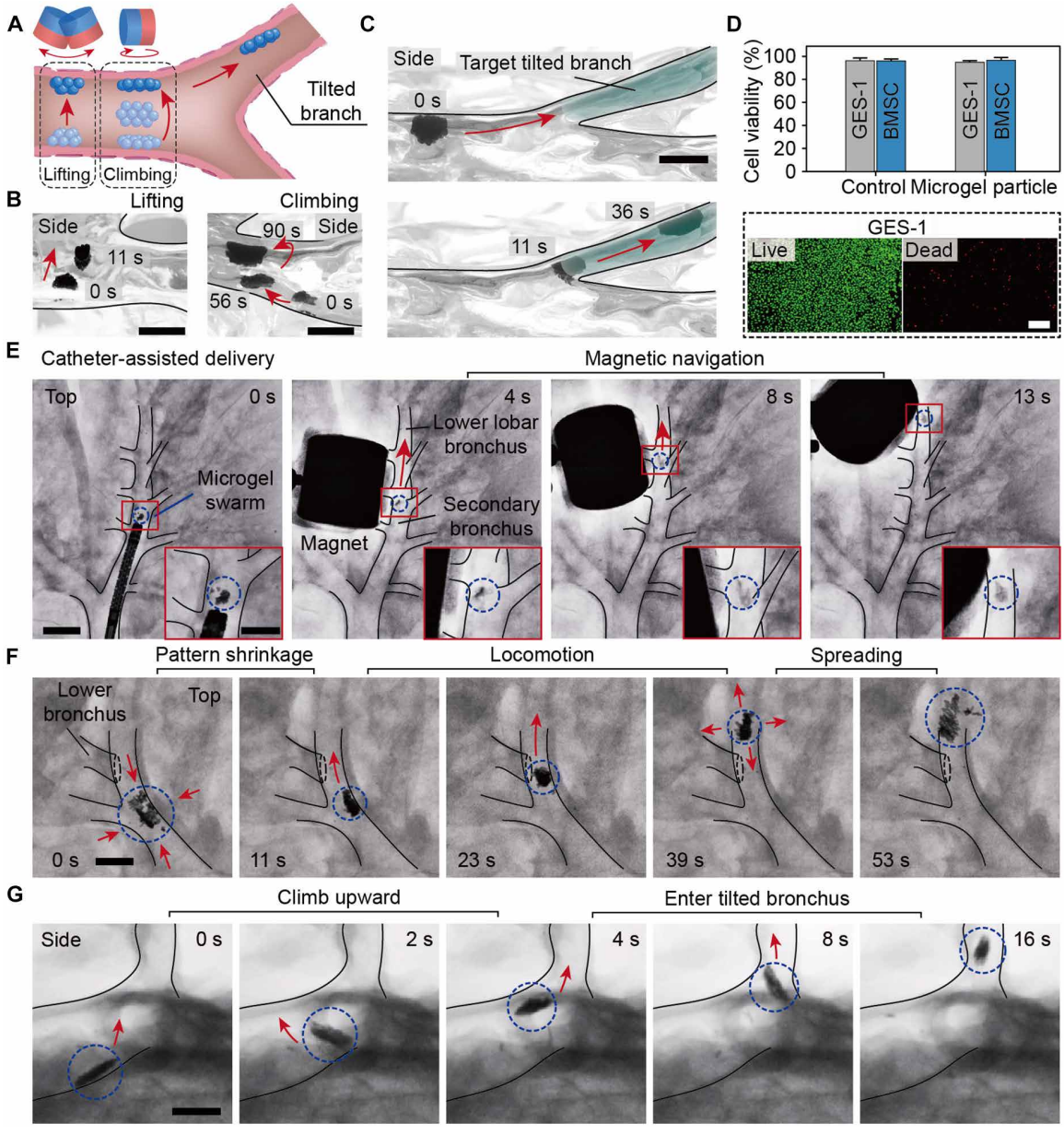

Fig. 5. Swarm navigation in in vitro and ex vivo bronchial trees. (**A**) Schematics of the swarm moving to the tilted branch. (**B**) A swarm moves from the bottom to the upper surface in the bronchus by lifting and climbing motions. Scale bars, 5 mm. (**C**) Swarm navigation to the upper tilted branch. The green area indicates the target tilted branch. Scale bar, 5 mm. (**D**) Viability of GES-1 and BMSCs after coculturing with the microgel particles. The control group indicates that only the cells are cultured. Scale bar, 500 μm. (**E**) Swarm delivery to the lower lobar bronchus in the ex vivo porcine lung under x-ray fluoroscopy. Scale bar, 2 cm; scale bar in the inset, 1 cm. (**F**) Swarm reconfiguration and locomotion in ex vivo porcine bronchi for avoiding particle loss into the lower bronchus. Scale bar, 1 cm. (**G**) Swarm climbing to the tilted bronchus in the ex vivo porcine lung. Scale bar, 1 cm. The black lines in (B), (C), and (E) to (G) indicate the boundaries of the bronchi. The error bars indicate the SD obtained from three trials.

and movie S4). By performing controllable locomotion at the upper surface, the swarm entered the tilted tertiary bronchus (highlighted by the green area, tilted angle, ~20°), as shown in Fig. 5C. The swarm could also move on the inner surface of main bronchus with longitudinal folds (fig. S24) and into the distal bronchiole (fig. S25). Meanwhile, the delivery of two swarms with a short distance was achieved (figs. S26 and S27 and Supplementary text S9).

The biocompatibility of the microgel particles was verified by co-culturing the gastric epithelial (GES-1) cells and mouse bone mesenchymal stem cells (BMSCs) with the particles, and the viability of the cells remained unaffected by the particles compared with the control groups (Fig. 5D). The image-guided navigation of the microgel particle swarms in an ex vivo porcine lung was realized (Fig. 5, E to G, and movie S5). The mucus layer in the ex vivo lung was kept. To track the swarms, tantalum microparticles (Ta; imaging contrast agents) were doped in the microgel particles for the imaging under x-ray fluoroscopy. Compared with the in vitro phantom, the soft tissue and mucus layer in the ex vivo bronchial tree bring challenges to the effective swarm control. Under x-ray fluoroscopy, the bronchial segments (highlighted by black lines in Fig. 5E) were distinguished from surrounding tissues for the real-time navigation of the swarms. A clinical bronchoscope with an inner catheter was first used to deploy the microgel particle swarm in a secondary bronchus. A rotating magnetic field was applied to actuate the swarm toward a lower lobar bronchus with a distance of 45 mm, from 4 to 13 s. When encountering a lower branch in the ex vivo bronchial tree, the swarm performed structure shrinkage to 0.45 times of the initial coverage area for the avoidance of particle loss into the lower branch and off-target delivery (Fig. 5F). Moreover, the targeted delivery of the swarm to a tilted branch in the ex vivo porcine lung was achieved (Fig. 5G). The boundary of the tilted branch is highlighted by black lines. Actuated by the rotating field, the swarm was transported from the bottom to the upper surface of the bronchus (0 to 4 s) and was subsequently navigated into the tilted branch at 16 s. When the swarm was actuated by the magnet with a slow velocity, it can move as an entity with few particles lost during the locomotion (fig. S28 and Supplementary text S10).

In vivo experiments of swarm actuation and delivery

The in vivo physiological environment of the lung is different from the ex vivo model. The mucus is secreted continuously in the bronchi in vivo, and the lung contracts and expands periodically during respiration, leading to challenges of realizing the intrabronchial targeted delivery of the microgel particle swarms. The schematics of the in vivo experiments in a living pig are demonstrated in Fig. 6A. The swarm was first deployed using a clinical catheter in a bronchoscope to the main bronchus of the porcine lung. Subsequently, the external dynamic magnetic fields were applied to remotely navigate the swarm in the lung. CT scan was applied to reconstruct the structure of the bronchial tree to plan the actuation mode of the swarm on the basis of the surrounding environment and to localize the 3D position of the swarm. The bronchoscope was also used to assist in observing and validating the swarm structure during the delivery process.

The deployment of the microgel particle swarm via the catheter was observed by the bronchoscope, and the CT image shows that the swarm was deployed at the main bronchus (Fig. 6B). The swarm was then navigated into deeper bronchi actuated by magnetic fields, and the navigation process of the swarm in a bronchial segment is shown in Fig. 6 (C and D) and movie S6. Two projected CT images with different observing directions of the bronchial segment are shown in the left and middle images of Fig. 6C, and on the basis of the CT images, the 3D structure of the bronchial segment is schematically illustrated (right image, Fig. 6C). The bronchial segment extends from the main bronchus to the secondary bronchus with four branches, indicated by a1, b1, c1, and d1. The experimental results of swarm delivery in the bronchial segment were presented, and the bronchoscope provided the vision feedback (Fig. 6D). From 0 to 7 s, the swarm was actuated by the magnetic field to move forward, passing by the branches a1, b1, and c1. When the swarm encountered the branch d1, it was reconfigured to change the structure and avoid the particles from dropping into the branch d1 (11 to 14 s). Furthermore, we transported a swarm to the tilted target bronchus while maintaining another swarm in the lower branch (Fig. 6E). The swarm climbed from the side wall to the upper surface in the bronchus (0 to 5 s), and it entered the target branch after performing controllable locomotion at the upper surface (5 to 25 s). During the process, the swarm in the lower branch was not affected. CT scanning was subsequently conducted to check the overall delivery results (Fig. 6E), and it was observed that the swarm (highlighted by the red circle) successfully entered the upper target branch, validating that the swarm had the capability of performing climbing motion and precise delivery along the bronchial wall in vivo.

The long-distance targeted delivery of the swarm into deep bronchi with CT imaging feedback was investigated, and the results are shown in Fig. 7 (A and B). The CT scanning was first conducted to reconstruct the overall structure of the bronchial tree (Fig. 7A). The delivery path of the swarm was planned (blue arrows), and cross sections I to III were defined (yellow dashed lines). A catheter was used to deliver the swarm to cross section I, and then magnetic fields were applied to actuate the swarm toward cross sections II and III. During the delivery process, CT scanning was performed at these three cross sections at 0, 5, 15, and 30 min. The results are shown in Fig. 7B. At 0 min, the CT images show the initial state of the three cross sections before the swarm delivery. After performing the catheter-assisted swarm deployment (5 min), the swarm showing as the white region in the CT image (highlighted by the blue circle) appeared at the bronchus in cross section I. Meanwhile, cross sections II and III maintained the same as the initial states. With the subsequent magnetic navigation, the image signal of the microgel particle swarm disappeared at cross section I and was detected at cross sections II and III at 15 and 30 min, respectively. The results indicate that the swarm left cross section I and was delivered to cross sections II and III with the magnetic actuation, revealing the effectiveness of the swarm delivery method to deep bronchi in vivo.

To validate the drug delivery capability of the microgel particle swarms, the microgel particles containing fluorescent dyes (DiD, red fluorescence) were applied as the swarm agents (Fig. 7C). The uneven distribution of fluorescent dye in microgel particles was resulted from the fluorescence blockage by the encapsulated magnetic microparticles. It can be observed from fig. S29 that fluorescent dye encapsulated in microgel particles was distributed uniformly. After the delivery, the lung tissues at the target site (cross section III) and nontarget site were collected and processed by hematoxylin and eosin (H&E) staining, and the staining and fluorescence images are shown in Fig. 7D and fig. S30. The red fluorescence that did not surround the bronchial boundary was caused by the diffusion of the released fluorescent dye (Fig. 7D). By comparing the merged image of target and nontarget sites (Fig. 7, D and E), the fluorescence intensity of the

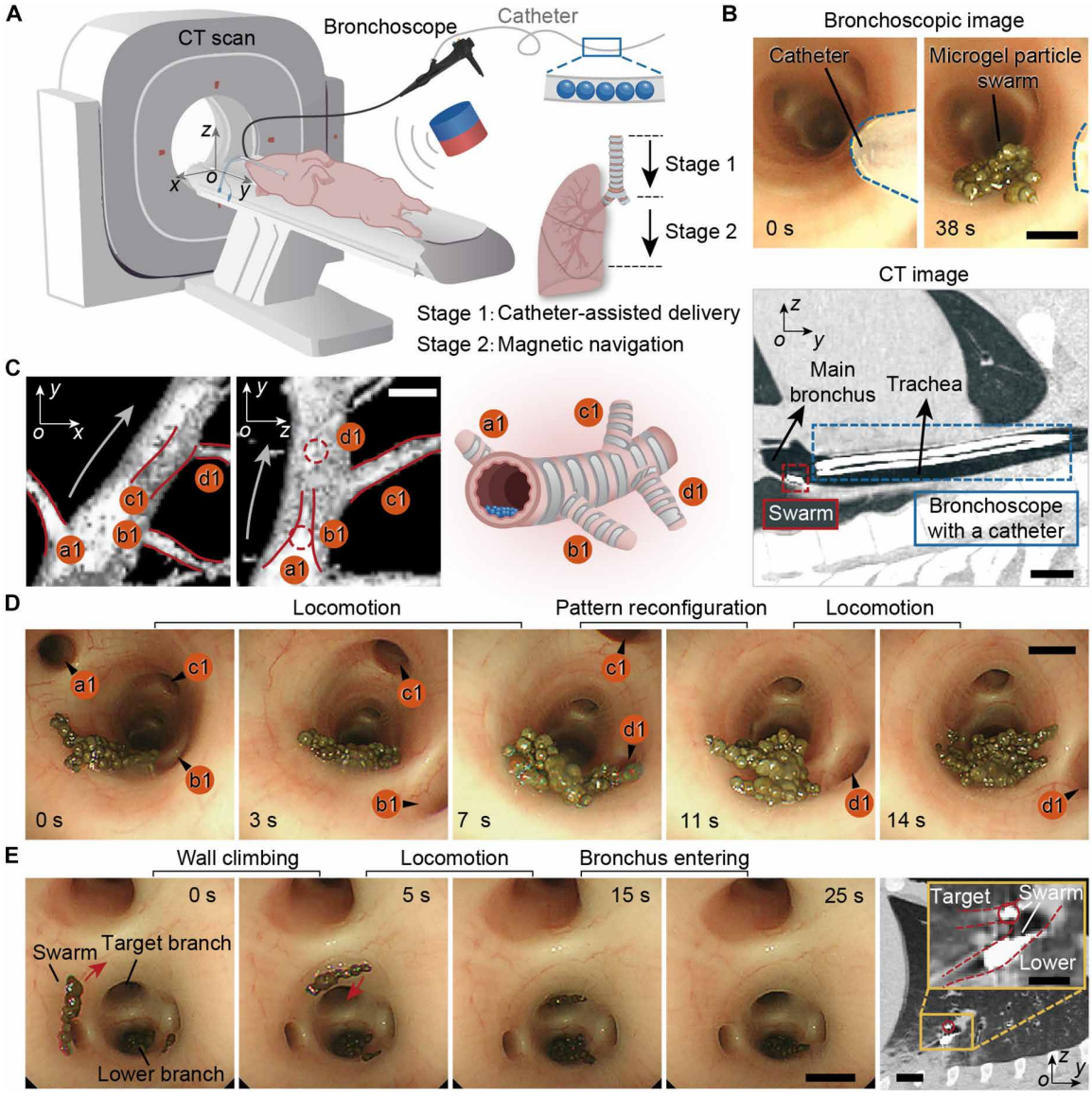

Fig. 6. Actuation of the microgel particle swarms in the in vivo porcine lung. (**A**) Schematics of the intrabronchial targeted delivery of the swarms in the lung in vivo. (**B**) Bronchoscopic and CT images showing the deployment of the swarm to the main bronchus of the porcine lung using a catheter. Scale bar in the bronchoscopic image, 2 mm; scale bar in the CT image, 2 cm. (**C**) CT image and schematic 3D structure of a bronchial segment with four branches, indicated by a1, b1, c1, and d1. The red lines indicate the boundaries of the bronchi, and the red dashed circles indicate the entrance of the invisible branches. The gray arrows indicate the planned movement direction of the swarm. Scale bar, 1 cm. (**D**) Swarm locomotion and reconfiguration in the bronchial segment. Scale bar, 2 mm. (**E**) Wall climbing and locomotion of a swarm to enter a tilted target branch. Scale bar, 2 mm. The CT image shows that the swarm enters the target branch. The red dashed lines indicate the boundaries of the bronchi. Scale bar in the CT image, 2 cm; scale bar in the inset, 1 cm.

delivered dye at the target site was significantly higher than that at the nontarget site. The quantitative comparison is also presented (Fig. 7F), indicating the effectiveness of intrabronchial targeted delivery using the microgel particle swarm into the deep bronchial tree. Furthermore, the safety of the microgel particles was validated by in vivo biosafety tests (fig. S31 and Supplementary text S11).

DISCUSSION

To date, intrabronchial pulmonary delivery of therapeutic agents is limited by the off-target accumulation to the normal lung tissues by inhalation and the low dexterity of clinical bronchoscopes in the narrow and tortuous bronchial tree. In this work, we developed magnetic microgel particle swarms with high locomotion dexterity and environmental adaptability, enabling the navigation and intrabronchial targeted delivery in the unstructured bronchial tree. Multimodal locomotion and reconfiguration of the swarms were achieved in constrained and air-filled environments. The swarms were controlled to pass through a tube while avoiding the holes in it and access the distal end of the simulated 3D human bronchial tree. Imaging contrast agents were encapsulated by the microgel particles to enable the medical imaging of the swarms, including x-ray fluoroscopy and CT

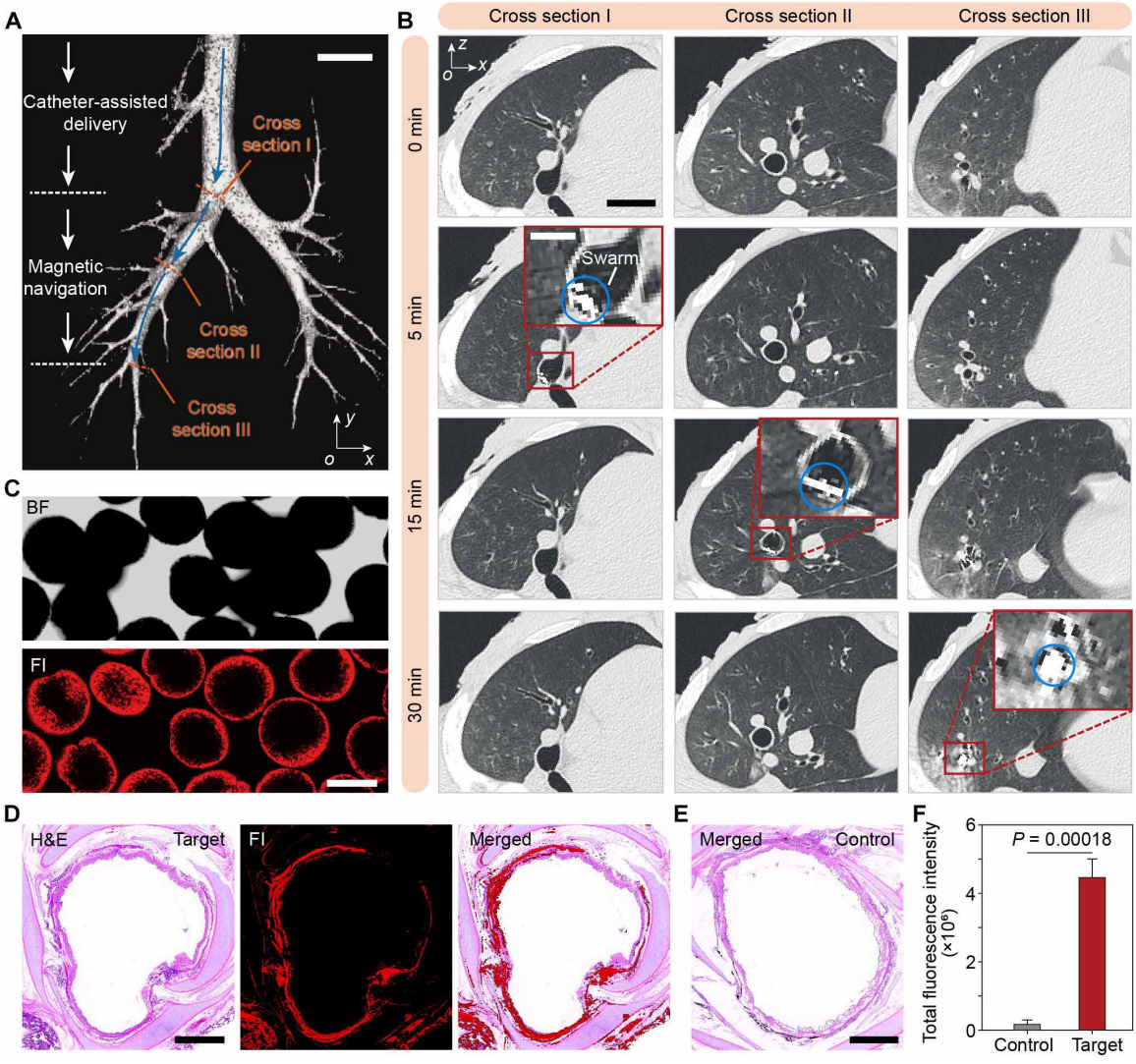

Fig. 7. Long-distance navigation and targeted delivery of the microgel particle swarms in the in vivo porcine lung. (**A**) CT image of the overall structure of the bronchial tree. The blue arrows show the planned navigation path of the swarm. Scale bar, 3 cm. (**B**) Results of CT scanning at the three cross sections during the delivery process and at 0, 5, 15, and 30 min. Scale bar, 3 cm. The insets are the enlarged views of the highlighted regions. Scale bar in the inset, 1 cm. (**C**) Bright-field (BF) and fluorescence (FI) images showing the swarms encapsulating red fluorescent dyes. Scale bar, 500 μm. (**D**) H&E staining, fluorescence, and merged images of the lung sample collected at the target site after the delivery process. Scale bar, 1 mm. (**E**) Merged image of the H&E staining and fluorescence images of the lung sample collected at the nontarget site after the delivery process as the control group. Scale bar, 1 mm. (**F**) Total fluorescence intensity of the lung samples at the target and nontarget sites. The error bars indicate the SD obtained from three trials.

imaging. In the ex vivo porcine lung, magnetic navigation of the swarms was achieved with the existence of a mucus layer under x-ray fluoroscopy. Moreover, with CT imaging feedback, in vivo delivery using the microgel particle swarms into the deep bronchi of a porcine lung was also achieved. In the in vivo environment, the swarm performed on-demand structure reconfiguration to avoid particle loss into nontarget branches, climbed along the bronchial wall to access the tilted branch, and successfully delivered the encapsulated fluorescent dye to the target site. This work enhances the understanding of swarm behaviors in nonfluidic environments and promises a method for pulmonary targeted delivery to treat lung diseases.

The bronchoscope was used to deploy microgel particle swarms to the lung. It is noted that the bronchoscope was widely used in clinical practices to deliver drugs. For example, gelatin and thrombin slurry were delivered through the working channel of the bronchoscope to treat patients with airway bleeding (*47*), and lipiodol was delivered through the bronchoscope to mark tumors and assist radiotherapy (*48*). Furthermore, microrobots can be delivered using clinical tools with similar working channels. For example, clinical catheters were used to deliver swarming microrobots to an aneurysm (*49*) and deploy a modularized microrobot to the bile duct (*50*). Endoscopy-assisted delivery of a helical microrobot to a tympanostomy tube in the middle ear was also reported (*51*).

The swarm swelling may cause airway blockage in small end branches. However, the potential risk to patients caused by the blockage is negligible. First, the microgel particle swarms were developed

to realize intrabronchial targeted delivery to deep bronchi, and therefore, even though the blockage occurs because of swarm swelling, it only affects a small portion of the lung. It is noted that bronchial occlusion is a common treatment procedure used in clinical practices (*52*, *53*). For patients with endobronchial bleeding, the main bronchus on the affected side of the lung shall be blocked to prevent blood from flowing into the unaffected side and to restrict airflow entering the damaged area (*53*). The bronchial occlusion in the lung of patients could last for 26 ± 13 hours (*53*), while the complete degradation time of the swarms is 180 min (fig. S7), which is substantially shorter.

After deploying swarms in the lung, the swarm was pulled against the bronchial wall. The gradient force applied on the swarm decreased from 4.8 to 0.041 mN with the increased distance to the magnet from 10 to 120 mm (fig. S14D). It is reported that the force causing airway trauma when using bougies was around 1000 mN (*54*), which is notably larger than the force applied on the bronchial wall exerted by the swarm. Therefore, the potential harm to the bronchial wall is negligible.

The swelling and degradation of swarms are triggered when they approach target sites. It has been reported that pH values of airway surface liquids in patients with pneumonia, pulmonary tuberculosis, and chronic bronchitis were around 7.2 to 7.4, 5.5 to 8.37, and 7.6 to 7.8, respectively (*55*–*57*). Therefore, the swelling and degradation behaviors of microgel particles could be triggered at the above disease sites to potentially play a role in treatment. Furthermore, in clinical practices, controlled dose of liquid could be injected into a small branch in a patient lung. For example, saline mixed with dornase alfa can be injected into the lung of patients to treat lobar atelectasis (*16*, *58*). As a result, for the cases when the particle swelling and degradation cannot occur autonomously, injection of alkaline liquid to local disease sites could be a solution. Moreover, it is noted that the microgel particles could be modulated to respond to acidic environments (*43*, *59*). Other stimulus-response swelling mechanisms of microgel particles have also been developed, such as temperature, light, and enzyme (*43*, *60*). Therefore, the microgel particles can further be tailored to swell and degrade according to actual physiological conditions of specific pulmonary diseases.

In animal trials, the swarm-magnet distance was ~7.5 cm (Fig. 7B), and at this distance, it was validated that the swarms could be actuated effectively for locomotion and structure reconfiguration (figs. S13 and S21). By further combining CT imaging feedback, precise control of the swarms in bronchi during the in vivo swarm delivery can be enabled through tuning of the motion of the magnet. When the tissue depth is larger than 7.5 cm, the demands of larger working distance of the applied magnetic field can be met by using magnets with larger sizes. Moreover, high-powered electromagnetic actuation devices with water-cooling systems (*61*) and a high concentration of magnetic particles can also be applied.

The disease treatment is the immediate next step, and before that, the following factors shall be considered. The target diseases and proper therapeutic agents should be determined as the first step. The drug release mode should be considered on the basis of specific demands. Moreover, if the sustained drug release over a relatively long period is required, the bioadhesion property shall further be integrated onto the microgel particles to increase their retention time in lungs and guarantee their stable adhesion on the targeted area during the dynamic expanding-contraction cycles of the lung. The long-term biosafety issue can be tackled from both aspects of materials and deployment methods. First, proper magnetic particles should be studied and explored. For example, the biocompatible and ferromagnetic nature of face-centered tetragonal iron platinum nanoparticles could be promising for targeted delivery in the lung (*62*, *63*). Moreover, retrieval strategies that can navigate the magnetic particles back after drug delivery at the diseased site are worthy of investigation. Meanwhile, the remanence of microgel particles used in this work and other existing microrobots is compared, as shown in table S1. The remanence of the proposed microgel particles is notably higher than that of microrobots using iron oxide nanoparticles and comparable to that of microrobots containing neodymium-iron-boron (NdFeB) particles. These results will guide the microrobot design when choosing alternative magnetic materials in the next step.

MATERIALS AND METHODS

Fabrication of magnetic microgel particles

First, a layer of silica was coated on the NdFeB microparticles through the Stöber process to reduce the cytotoxicity of the synthesized microgel particles (*64*). Briefly, 4% (w/v) NdFeB microparticles (5 μm in diameter, MQFP-B-2007609-089, Magnequench), 6% (v/v) ammonium hydroxide (29%, Aladdin), and 0.2% (v/v) tetraethyl orthosilicate (Sigma-Aldrich) were added into ethanol (Aladdin), and meanwhile, the mixture was stirred mechanically at 1500 rpm to prevent the NdFeB microparticles from sedimentation. After stirring for 12 hours, the microparticles were washed multiple times using acetone (Guangzhou Chemical Reagent Factory). Last, SiO_2-coated NdFeB microparticles were obtained through vacuum filtrations of the suspension. The remanence and coercivity of SiO_2-coated NdFeB particles are almost 79.3 emu/g and 8.3 kOe, respectively (fig. S32). With the prepared SiO_2-coated NdFeB microparticles, magnetic microgel particles were synthesized through an extrusion-dripping method (fig. S33). Briefly, 1% (w/w) sodium alginate (Aladdin) and 6% (w/w) NdFeB microparticles were mixed into deionized water as the precursor. After mechanical stirring for 6 hours, the precursor was fully dissolved and then was added to a syringe. A pump (LSP02-3B, Ditron Electronic Technology Co., Ltd.) was applied to propel the fluid in the syringe at a constant speed to extrude droplets of the precursor into a solution of 5% (w/w) $CaCl_2$ (Aladdin), triggering the polymerization reaction of the hydrogel precursor. The droplets were thus solidified into microgel particles. The fabricated microgel particles were initially stored in deionized water. Before the experiments, the microgel particles were taken out from water, and during the experiments, no additional solution was added. The swarm size was controlled by adjusting the size and number of microgel particles. Meanwhile, the size of microgel particles was controlled by changing the extrusion rate and size of the needle on the syringe.

Setup for experiments

The microgel particles were actuated by a cylindrical permanent magnet with a height of 50 mm and a diameter of 50 mm, which was integrated with a motor, and installed on a robot arm (CR5, Dobot Robotics) (fig. S34). During in vitro experiments, a home-made platform was placed on the optical table and integrated with a top camera and a side camera (Alpha a6400, Sony Electronics Corporation). On the platform, a glass sheet was placed as the substrate. At the current stage, we operated the system with a human in the loop. The magnetic control of the swarms was accomplished by a human

operator. Specifically, the motor connected to the magnet was controlled by an Arduino interface running a custom-made program. The field rotation and oscillation were controlled by manually adjusting motor parameters in the program. The position and pose of the robot arm attaching the magnet were tuned manually via a DobotStudio interface. The simulated human 3D bronchial tree (fig. S35A) was purchased from a medical phantom company (Trandomed 3D Medical Technology Co.). The diameter of the branches in the bronchial tree phantom is shown in fig. S35B.

Particle characterization

The optical image of the microgel particles was obtained using a digital camera (Alpha a6400, Sony Electronics Corporation). The SEM image and the energy-dispersive x-ray analysis image of the microgel particles were obtained using a scanning electron microscope (MIRA LMS, TESCAN). The hysteresis loop of the microgel particles was measured by a vibrating sample magnetometer (7404, Lake Shore Cryotronics Inc.). The size distribution of the microgel particles was analyzed using ImageJ.

Swelling, degradation, and release test

Four environments with different pH values of 9.8, 7.4, 6.8, and 2.7 were prepared and measured using a pH portable multiparameter meter (Orion Star A324, Thermo Fisher Scientific). The microgel particles were immersed in the four fluidic environments, and the swelling and degradation of the microgel particles were observed using an inverted fluorescent microscope (ECLIPSE Ti2, Nikon Corporation). The particle diameter was quantified using ImageJ and MATLAB. For the swarm degradation experiments in fig. S8, the microgel particle swarms under magnetic fields were used. For the sustained release test, the microgel particles containing DOX (Aladdin) were immersed in 10 mL deionized water and shaken on a shaker (OS-40Pro, JOANLAB). Every 12 hours, 1 mL of the suspension was sampled and replaced. The DOX concentration of the sampled suspension was obtained by a UV-vis spectrophotometer (UV-1900i, Shimadzu).

Cell viability test

The GES-1 cells (Xiamen Immocell Biotechnology Co., Ltd.) and mouse BMSCs (Xiamen Immocell Biotechnology Co., Ltd.) were used to assess the biocompatibility of the microgel particles. Briefly, the GES-1 cells and BMSCs were incubated with the microgel particles in 96-well plates for 24 hours. Subsequently, all cell samples within each well were stained with calcein acetoxymethyl ester (calcein AM) and ethidium homodimer (Sigma-Aldrich) for 30 min. Fluorescence images of the stained cells were captured using an inverted fluorescent microscope (ECLIPSE Ti2, Nikon Corporation) and then analyzed using ImageJ. The GES-1 cells and BMSCs without microgel particles were used as control groups for cell viability test.

Simulation procedure

We performed a simulation of the swarm reconfiguration in COMSOL Multiphysics. The magnetic dipolar interaction, capillary interactions, gravitational force, particle-particle excluded volume force, and repulsive force between the particles and the substrate were simulated using the dynamic mode in Supplementary text S7. The used parameters are shown in table S2. The diameter of the particles is 650 μm. The density of the particles is 1500 kg/m^3. The field frequency f is 1 Hz. The viscosity and density of air are defined as 1.81×10^{-5} Pa s and 1.293 kg/m^3, respectively.

Ex vivo experiment

The porcine lungs were provided by a local slaughterhouse within 48 hours. During transportation, these organs were stored with ice (~2°C) to delay metamorphosis. The lungs were gently and minimally cleaned by water to reduce the damage to the mucus layer. When conducting the swarm delivery in the ex vivo porcine lungs, the tantalum microparticles (5 μm, Aladdin) were contained in the microgel particles for imaging under x-ray fluoroscopy (Pilot 3000, Beijing WeMed Medical Technology Co., Ltd.). Porcine lung tissue and the microgel particles with different Ta microparticle concentrations were prepared and observed under x-ray fluoroscopy (fig. S36A). The fluoroscopy imaging contrast was enhanced with the increase in Ta concentration. The quantitative comparison was also conducted through the calculated mean grayscale value of the fluoroscopy images (fig. S36B). The grayscale value decreased from 93.68 to 74.52 with an increase in Ta concentration from 0 to 15% (w/v) and then leveled out. Meanwhile, the grayscale value of porcine lung tissue was 87.13, which was larger than that of microgel particles with a concentration of 15% (w/v). This result indicates that the microgel particle swarms with a Ta concentration of 15% (w/v) was able to be detected in a porcine lung, and thus, a 15% (w/v) Ta concentration was selected for the following experiments. A clinical catheter within a bronchoscope (outer diameter, 5.9 mm; inner channel diameter, 2.8 mm; EB-530T, FUJINON Corporation) was used to deliver the swarm to the bronchus. The subsequent real-time magnetic navigation of the swarm was also conducted under x-ray fluoroscopy.

In vivo experiment

The animal trial was approved by the Institutional Animal Care and Use Committee with license number SYXK2023-0316. In the CT scan room, a 7-month-old male domestic pig (~65 kg in weight) was placed on the table, and the anesthesia and oxygen inhalation were maintained throughout the experiments. With the pig in a supine position, an endotracheal tube was placed through the mouth to the trachea, and a bronchoscope (outer diameter, 5.9 mm; inner channel diameter, 2.8 mm; BF-1T260, Olympus Corporation) was inserted into the porcine main bronchus through the endotracheal tube. The reconstruction of the bronchial structure and swarm localization were realized using the CT scanner (Incisive CT, Philips). The diameters of cross sections I to III were almost 14.9, 12.6, and 4.2 mm, respectively. During the experiments, the actuation system was placed near the CT scanner. The magnetic navigation and CT scan were performed alternately. After swarm navigation, the positions of the magnet and the operation table holding the animal were first recorded. The magnet was then slowly moved away by the robot arm, and the operation table was moved to send the animal for CT scanning. The swarm position in the lung and the subsequent delivery path were thus determined. After the scanning, the operation table and the magnet were sequentially moved back to their latest recorded positions. The swarm was subsequently propelled by the magnet. The microgel particle swarm was fixed by placing an external magnet, and the release of encapsulated fluorescent dye at the target site was achieved. The results proved that the influences of pulmonary clearance mechanisms on the particle position could be negligible in this case. After experiments, the pig was euthanized and the lung samples at the target and nontarget sites were collected for histology investigation. The samples were treated with 4% polyformaldehyde (P0099, Beyotime Biotechnology) for 48 hours and

then were embedded in paraffin after washing. Using a microtome (RM2016, Leica), the samples were sliced into sections with a thickness of 4 μm and stained with H&E assay. The samples were imaged using a digital slide scanner (Pannoramic, 3DHISTECH).

Statistical tests

Experimental values were obtained from three trials, and the results are presented as the means ± SD. Differences between experimental data are evaluated using Student's t test. $P < 0.001$ is considered as significantly different.

Supplementary Materials

The PDF file includes:

Figs. S1 to S36
Supplementary Text S1 to S11
Tables S1 and S2
Legends for movies S1 to S6
References

Other Supplementary Material for this manuscript includes the following:

Movies S1 to S6

REFERENCES AND NOTES

1. M. Wang, R. S. Herbst, C. Boshoff, Toward personalized treatment approaches for non-small-cell lung cancer. *Nat. Med.* **27**, 1345–1356 (2021).
2. N. Kirchhammer, M. P. Trefny, P. Auf Der Maur, H. Läubli, A. Zippelius, Combination cancer immunotherapies: Emerging treatment strategies adapted to the tumor microenvironment. *Sci. Transl. Med.* **14**, eabo3605 (2022).
3. L. Allen, L. Allen, S. B. Carr, G. Davies, D. Downey, M. Egan, J. T. Forton, R. Gray, C. Haworth, A. Horsley, A. R. Smyth, K. W. Southern, J. C. Davies, Future therapies for cystic fibrosis. *Nat. Commun.* **14**, 693 (2023).
4. L. M. Rose, R. Neale, Development of the first inhaled antibiotic for the treatment of cystic fibrosis. *Sci. Transl. Med.* **2**, 63mr4 (2010).
5. F. Zhang, J. Zhuang, Z. Li, H. Gong, B. E.-F. de Ávila, Y. Duan, Q. Zhang, J. Zhou, L. Yin, E. Karshalev, W. Gao, V. Nizet, R. H. Fang, L. Zhang, J. Wang, Nanoparticle-modified microrobots for in vivo antibiotic delivery to treat acute bacterial pneumonia. *Nat. Mater.* **21**, 1324–1332 (2022).
6. A. Schäfer, D. R. Martinez, J. J. Won, R. M. Meganck, F. R. Moreira, A. J. Brown, K. L. Gully, M. R. Zweigart, W. S. Conrad, S. R. May, S. Dong, R. Kalla, K. Chun, V. Du Pont, D. Babusis, J. Tang, E. Murakami, R. Subramanian, K. T. Barrett, B. J. Bleier, R. Bannister, J. Y. Feng, J. P. Bilello, T. Cihlar, R. L. Mackman, S. A. Montgomery, R. S. Baric, T. P. Sheahan, Therapeutic treatment with an oral prodrug of the remdesivir parental nucleoside is protective against SARS-CoV-2 pathogenesis in mice. *Sci. Transl. Med.* **14**, eabm3410 (2022).
7. S. Wilhelm, A. J. Tavares, Q. Dai, S. Ohta, J. Audet, H. F. Dvorak, W. C. W. Chan, Analysis of nanoparticle delivery to tumours. *Nat. Rev. Mater.* **1**, 16014 (2016).
8. J. Kim, Y. Eygeris, R. C. Ryals, A. Jozić, G. Sahay, Strategies for non-viral vectors targeting organs beyond the liver. *Nat. Nanotechnol.* **19**, 428–447 (2024).
9. R. S. Riley, C. H. June, R. Langer, M. J. Mitchell, Delivery technologies for cancer immunotherapy. *Nat. Rev. Drug Discov.* **18**, 175–196 (2019).
10. M. Liu, S. Hu, N. Yan, K. D. Popowski, K. Cheng, Inhalable extracellular vesicle delivery of IL-12 mRNA to treat lung cancer and promote systemic immunity. *Nat. Nanotechnol.* **19**, 565–575 (2024).
11. M. T. Manzari, Y. Shamay, H. Kiguchi, N. Rosen, M. Scaltriti, D. A. Heller, Targeted drug delivery strategies for precision medicines. *Nat. Rev. Mater.* **6**, 351–370 (2021).
12. M. J. Mitchell, M. M. Billingsley, R. M. Haley, M. E. Wechsler, N. A. Peppas, R. Langer, Engineering precision nanoparticles for drug delivery. *Nat. Rev. Drug Discov.* **20**, 101–124 (2021).
13. A. Suberi, M. K. Grun, T. Mao, B. Israelow, M. Reschke, J. Grundler, L. Akhtar, T. Lee, K. Shin, A. S. Piotrowski-Daspit, R. J. Homer, A. Iwasaki, H.-W. Suh, W. M. Saltzman, Polymer nanoparticles deliver mRNA to the lung for mucosal vaccination. *Sci. Transl. Med.* **15**, eabq0603 (2023).
14. Q.-F. Meng, W. Tai, M. Tian, X. Zhuang, Y. Pan, J. Lai, Y. Xu, Z. Xu, M. Li, G. Zhao, G.-T. Yu, G. Yu, R. Chen, N. Jin, X. Li, G. Cheng, X. Chen, L. Rao, Inhalation delivery of dexamethasone with iSEND nanoparticles attenuates the COVID-19 cytokine storm in mice and nonhuman primates. *Sci. Adv.* **9**, eadg3277 (2023).
15. L. Yang, C. Yang, N. Wan, W. Xie, Y. Tian, Y. Xiao, L. Luo, E. Chen, J. Zhang, X. Wang, L. Xu, X. Wang, Y. Zhou, L. Guo, J. Zou, X. Liu, X. Wei, Y. Wang, J. Feng, Bronchoscopic instillation of amphotericin B is a safe and effective measure to treat pulmonary mycosis. *Front. Pharmacol.* **14**, 1167475 (2023).
16. H. Assallum, T. Y. Song, L. DeLorenzo, K. Harris, Bronchoscopic instillation of DNase to manage refractory lobar atelectasis in a lung cancer patient. *Ann. Transl. Med.* **7**, 363–363 (2019).
17. A. DeMaio, D. Sterman, Bronchoscopic intratumoural therapies for non-small cell lung cancer. *Eur. Respir. Rev.* **29**, 200028 (2020).
18. M. Oki, H. Saka, Diagnostic value of ultrathin bronchoscopy in peripheral pulmonary lesions: A narrative review. *J. Thorac. Dis.* **12**, 7675–7682 (2020).
19. Z. Mitros, B. Thamo, C. Bergeles, L. Da Cruz, K. Dhaliwal, M. Khadem, Design and modelling of a continuum robot for distal lung sampling in mechanically ventilated patients in critical care. *Front. Robot. AI* **8**, 611866 (2021).
20. E. R. Weibel, *Morphometry of the Human Lung* (Springer Berlin Heidelberg, 1963); http://link.springer.com/10.1007/978-3-642-87553-3.
21. B. J. Nelson, S. Pané, Delivering drugs with microrobots. *Science* **382**, 1120–1122 (2023).
22. B. Wang, Q. Wang, K. Chan, Z. Ning, Q. Wang, F. Ji, H. Yang, S. Jiang, Z. Zhang, B. Y. M. Ip, H. Ko, J. P. W. Chung, M. Qiu, J. Han, P. W. Y. Chiu, J. J. Y. Sung, S. Du, T. W. H. Leung, S. C. H. Yu, L. Zhang, tPA-anchored nanorobots for in vivo arterial recanalization at submillimeter-scale segments. *Sci. Adv.* **10**, eadk8970 (2024).
23. C. Simó, M. Serra-Casablancas, A. C. Hortelao, V. D. Carlo, S. Guallar-Garrido, S. Plaza-García, R. M. Rabanal, P. Ramos-Cabrer, B. Yagüe, L. Aguado, L. Bardia, S. Tosi, V. Gomez-Vallejo, A. Martín, T. Patiño, E. Julián, J. Colombelli, J. Llop, S. Sánchez, Urease-powered nanobots for radionuclide bladder cancer therapy. *Nat. Nanotechnol.* **19**, 554–564 (2024).
24. F. Zhang, Z. Li, Y. Duan, A. Abbas, R. Mundaca-Uribe, L. Yin, H. Luan, W. Gao, R. H. Fang, L. Zhang, J. Wang, Gastrointestinal tract drug delivery using algae motors embedded in a degradable capsule. *Sci. Robot.* **7**, eabo4160 (2022).
25. H. Gu, E. Hanedan, Q. Boehler, T.-Y. Huang, A. J. T. M. Mathijssen, B. J. Nelson, Artificial microtubules for rapid and collective transport of magnetic microcargoes. *Nat. Mach. Intell.* **4**, 678–684 (2022).
26. G.-Z. Yang, J. Bellingham, P. E. Dupont, P. Fischer, L. Floridi, R. Full, N. Jacobstein, V. Kumar, M. McNutt, R. Merrifield, B. J. Nelson, B. Scassellati, M. Taddeo, R. Taylor, M. Veloso, Z. L. Wang, R. Wood, The grand challenges of *Science Robotics*. *Sci. Robot.* **3**, eaar7650 (2018).
27. J. Yu, D. Jin, K.-F. Chan, Q. Wang, K. Yuan, L. Zhang, Active generation and magnetic actuation of microrobotic swarms in bio-fluids. *Nat. Commun.* **10**, 5631 (2019).
28. Z. Wu, Y. Chen, D. Mukasa, O. S. Pak, W. Gao, Medical micro/nanorobots in complex media. *Chem. Soc. Rev.* **49**, 8088–8112 (2020).
29. Y. Wang, H. Chen, L. Xie, J. Liu, L. Zhang, J. Yu, Swarm autonomy: From agent functionalization to machine intelligence. *Adv. Mater.* **37**, 2312956 (2024).
30. H. Xie, M. Sun, X. Fan, Z. Lin, W. Chen, L. Wang, L. Dong, Q. He, Reconfigurable magnetic microrobot swarm: Multimode transformation, locomotion, and manipulation. *Sci. Robot.* **4**, eaav8006 (2019).
31. M. Sun, S. Yang, J. Jiang, S. Jiang, M. Sitti, L. Zhang, Bioinspired self-assembled colloidal collectives drifting in three dimensions underwater. *Sci. Adv.* **9**, eadj4201 (2023).
32. L. Yang, J. Jiang, X. Gao, Q. Wang, Q. Dou, L. Zhang, Autonomous environment-adaptive microrobot swarm navigation enabled by deep learning-based real-time distribution planning. *Nat. Mach. Intell.* **4**, 480–493 (2022).
33. Q. Wang, K. F. Chan, K. Schweizer, X. Du, D. Jin, S. C. H. Yu, B. J. Nelson, L. Zhang, Ultrasound Doppler-guided real-time navigation of a magnetic microswarm for active endovascular delivery. *Sci. Adv.* **7**, eabe5914 (2021).
34. Q. Wang, Q. Wang, Z. Ning, K. F. Chan, J. Jiang, Y. Wang, L. Su, S. Jiang, B. Wang, B. Y. M. Ip, H. Ko, T. W. H. Leung, P. W. Y. Chiu, S. C. H. Yu, L. Zhang, Tracking and navigation of a microswarm under laser speckle contrast imaging for targeted delivery. *Sci. Robot.* **9**, eadh1978 (2024).
35. P. Wrede, O. Degtyaruk, S. K. Kalva, X. L. Deán-Ben, U. Bozuyuk, A. Aghakhani, B. Akolpoglu, M. Sitti, D. Razansky, Real-time 3D optoacoustic tracking of cell-sized magnetic microrobots circulating in the mouse brain vasculature. *Sci. Adv.* **8**, eabm9132 (2022).
36. H. Chen, H. Zhang, T. Xu, J. Yu, An overview of micronanoswarms for biomedical applications. *ACS Nano* **15**, 15625–15644 (2021).
37. M. Yang, Y. Zhang, F. Mou, C. Cao, L. Yu, Z. Li, J. Guan, Swarming magnetic nanorobots bio-interfaced by heparinoid-polymer brushes for in vivo safe synergistic thrombolysis. *Sci. Adv.* **9**, eadk7251 (2023).
38. G. Go, S.-G. Jeong, A. Yoo, J. Han, B. Kang, S. Kim, K. T. Nguyen, Z. Jin, C.-S. Kim, Y. R. Seo, J. Y. Kang, J. Y. Na, E. K. Song, Y. Jeong, J. K. Seon, J.-O. Park, E. Choi, Human adipose–derived mesenchymal stem cell–based medical microrobot system for knee cartilage regeneration in vivo. *Sci. Robot.* **5**, eaay6626 (2020).
39. Z. Wu, J. Troll, H.-H. Jeong, Q. Wei, M. Stang, F. Ziemssen, Z. Wang, M. Dong, S. Schnichels, T. Qiu, P. Fischer, A swarm of slippery micropropellers penetrates the vitreous body of the eye. *Sci. Adv.* **4**, eaat4388 (2018).

40. T. Li, S. Yu, B. Sun, Y. Li, X. Wang, Y. Pan, C. Song, Y. Ren, Z. Zhang, K. T. V. Grattan, Z. Wu, J. Zhao, Bioinspired claw-engaged and biolubricated swimming microrobots creating active retention in blood vessels. *Sci. Adv.* **9**, eadg4501 (2023).
41. G. Go, A. Yoo, K. T. Nguyen, M. Nan, B. A. Darmawan, S. Zheng, B. Kang, C.-S. Kim, D. Bang, S. Lee, K.-P. Kim, S. S. Kang, K. M. Shim, S. E. Kim, S. Bang, D.-H. Kim, J.-O. Park, E. Choi, Multifunctional microrobot with real-time visualization and magnetic resonance imaging for chemoembolization therapy of liver cancer. *Sci. Adv.* **8**, eabq8545 (2022).
42. J. Law, X. Wang, M. Luo, L. Xin, X. Du, W. Dou, T. Wang, G. Shan, Y. Wang, P. Song, X. Huang, J. Yu, Y. Sun, Microrobotic swarms for selective embolization. *Sci. Adv.* **8**, eabm5752 (2022).
43. J. Li, D. J. Mooney, Designing hydrogels for controlled drug delivery. *Nat. Rev. Mater.* **1**, 16071 (2016).
44. Z. Zhao, A. Ukidve, Y. Gao, J. Kim, S. Mitragotri, Erythrocyte leveraged chemotherapy (ELeCt): Nanoparticle assembly on erythrocyte surface to combat lung metastasis. *Sci. Adv.* **5**, eaax9250 (2019).
45. S. Sengupta, D. Eavarone, I. Capila, G. Zhao, N. Watson, T. Kiziltepe, R. Sasisekharan, Temporal targeting of tumour cells and neovasculature with a nanoscale delivery system. *Nature* **436**, 568–572 (2005).
46. T. Yong, X. Zhang, N. Bie, H. Zhang, X. Zhang, F. Li, A. Hakeem, J. Hu, L. Gan, H. A. Santos, X. Yang, Tumor exosome-based nanoparticles are efficient drug carriers for chemotherapy. *Nat. Commun.* **10**, 3838 (2019).
47. A. R. Peralta, M. Chawla, R. P. Lee, Novel bronchoscopic management of airway bleeding with absorbable gelatin and thrombin slurry. *J. Bronchol. Interv. Pulmonol.* **25**, 204–211 (2018).
48. M. Rose, S. Siva, D. Ball, L. B. Irving, D. P. Steinfort, Bronchoscopic delivery of lipiodol as a fiducial marker in lung tumors before radiotherapy. *J. Thorac. Oncol.* **9**, 1579–1583 (2014).
49. D. Jin, Q. Wang, K. F. Chan, N. Xia, H. Yang, Q. Wang, S. C. H. Yu, L. Zhang, Swarming self-adhesive microgels enabled aneurysm on-demand embolization in physiological blood flow. *Sci. Adv.* **9**, eadf9278 (2023).
50. L. Su, D. Jin, Y. Wang, Q. Wang, C. Pan, S. Jiang, H. Yang, Z. Yang, X. Wang, N. Xia, K. F. Chan, P. W. Y. Chiu, J. J.-Y. Sung, L. Zhang, Modularized microrobot with lock-and-detachable modules for targeted cell delivery in bile duct. *Sci. Adv.* **9**, eadj0883 (2023).
51. Y. Dong, L. Wang, Z. Zhang, F. Ji, T. K. F. Chan, H. Yang, C. P. L. Chan, Z. Yang, Z. Chen, W. T. Chang, J. Y. K. Chan, J. J. Y. Sung, L. Zhang, Endoscope-assisted magnetic helical micromachine delivery for biofilm eradication in tympanostomy tube. *Sci. Adv.* **8**, eabq8573 (2022).
52. T. Sakaguchi, H. Kida, Y. Kanno, B. Oyama, T. Inoue, T. Miyazawa, M. Mineshita, Bronchial occlusion with endobronchial watanabe spigot for hemoptysis in a mechanically ventilated patient with extracorporeal circulation. *Intern. Med.* **58**, 267–269 (2019).
53. N. Nishiumi, T. Nakagawa, R. Masuda, M. Iwasaki, S. Inokuchi, H. Inoue, Endobronchial bleeding associated with blunt chest trauma treated by bronchial occlusion with a univent. *Ann. Thorac. Surg.* **85**, 245–250 (2008).
54. B. A. Marson, E. Anderson, A. R. Wilkes, I. Hodzovic, Bougie-related airway trauma: Dangers of the hold-up sign. *Anaesthesia* **69**, 219–223 (2014).
55. H. Fischer, J. H. Widdicombe, Mechanisms of acid and base secretion by the airway epithelium. *J. Membr. Biol.* **211**, 139–150 (2010).
56. M. Masuda, T. Sato, K. Sakamaki, M. Kudo, T. Kaneko, Y. Ishigatsubo, The effectiveness of sputum pH analysis in the prediction of response to therapy in patients with pulmonary tuberculosis. *PeerJ* **3**, e1448 (2015).
57. K. Adler, O. Wooten, W. Philippoff, E. Lerner, M. J. Dulfano, Physical properties of sputum: III. Rheologic variability and intrinsic relationships. *Am. Rev. Respir. Dis.* **106**, 86–96 (1972).
58. D. M. Slattery, D. A. Waltz, B. Denham, M. O'Mahony, P. Greally, Bronchoscopically administered recombinant human DNase for lobar atelectasis in cystic fibrosis. *Pediatr. Pulmonol.* **31**, 383–388 (2001).
59. M. Kanamala, W. R. Wilson, M. Yang, B. D. Palmer, Z. Wu, Mechanisms and biomaterials in pH-responsive tumour targeted drug delivery: A review. *Biomaterials* **85**, 152–167 (2016).
60. A. C. Daly, L. Riley, T. Segura, J. A. Burdick, Hydrogel microparticles for biomedical applications. *Nat. Rev. Mater.* **5**, 20–43 (2019).
61. X. Du, J. Yu, Image-integrated magnetic actuation systems for localization and remote actuation of medical miniature robots: A survey. *IEEE Trans. Robot.* **39**, 2549–2568 (2023).
62. V. M. Kadiri, C. Bussi, A. W. Holle, K. Son, H. Kwon, G. Schütz, M. G. Gutierrez, P. Fischer, Biocompatible magnetic micro- and nanodevices: Fabrication of FePt nanopropellers and cell transfection. *Adv. Mater.* **32**, 2001114 (2020).
63. J. Giltinan, V. Sridhar, U. Bozuyuk, D. Sheehan, M. Sitti, 3D microprinting of iron platinum nanoparticle-based magnetic mobile microrobots. *Adv. Intell. Syst.* **3**, 2000204 (2021).
64. Y. Kim, G. Parada, S. Liu, X. Zhao, Ferromagnetic soft continuum robots. *Sci. Robot.* **4**, eaax7329 (2019).
65. K. W. Yung, P. B. Landecker, D. D. Villani, An analytic solution for the force between two magnetic dipoles. *Magn. Electr. Sep.* **9**, 39–52 (1970).
66. Y. Gao, M. A. Hulsen, T. G. Kang, J. M. J. den Toonder, Numerical and experimental study of a rotating magnetic particle chain in a viscous fluid. *Phys. Rev. E* **86**, 041503 (2012).
67. H.-J. Butt, M. Kappl, Normal capillary forces. *Adv. Colloid Interface Sci.* **146**, 48–60 (2009).
68. I. Gudavadze, E.-L. Florin, Normal capillary forces on a spherical particle protruding from a thin liquid film and its application to swarming bacteria. *Colloids Surf. A Physicochem. Eng. Asp.* **636**, 128176 (2022).
69. S. Melle, O. G. Calderón, M. A. Rubio, G. G. Fuller, Microstructure evolution in magnetorheological suspensions governed by Mason number. *Phys. Rev. E* **68**, 041503 (2003).
70. S. Krishnamurthy, A. Yadav, P. E. Phelan, R. Calhoun, A. K. Vuppu, A. A. Garcia, M. A. Hayes, Dynamics of rotating paramagnetic particle chains simulated by particle dynamics, Stokesian dynamics and lattice Boltzmann methods. *Microfluid. Nanofluidics* **5**, 33–41 (2008).
71. F. Martinez-Pedrero, P. Tierno, Magnetic propulsion of self-assembled colloidal carpets: Efficient cargo transport via a conveyor-belt effect. *Phys. Rev. Appl.* **3**, 051003 (2015).
72. C. Karamaoun, B. Sobac, B. Mauroy, A. Van Muylem, B. Haut, New insights into the mechanisms controlling the bronchial mucus balance. *PLOS ONE* **13**, e0199319 (2018).
73. G. A. Duncan, J. Jung, J. Hanes, J. S. Suk, The mucus barrier to inhaled gene therapy. *Mol. Ther.* **24**, 2043–2053 (2016).
74. J. Huang, Y. Liu, J. Wu, F. Dong, C. Liu, J. Luo, X. Liu, N. Wang, L. Wang, H. Xu, An extracellular matrix-mimicking magnetic microrobot for targeted elimination of circulating cancer cells. *Nanoscale* **16**, 624–634 (2024).

Acknowledgments: We thank Y. C. Zhang for the help on swarm maneuver and control. **Funding:** This work was supported by the following: National Key R&D Program of China under project no. 2022YFA1207100, National Natural Science Foundation of China under project no. 62103347, Guangdong Basic and Applied Basic Research Foundation under project no. 2022A1515110499, Shenzhen Institute of Artificial Intelligence and Robotics for Society under project no. BN00202312037-1D, China Merchants Group funding under project no. BN00202312037, and Longang District Shenzhen's "Ten Action Plan" under project no. LGKCSDPT 2024002 and 2024003. **Author contributions:** H.C., Z.W., F.D., Y.S., and J.Y. conceived the project and designed the experiments. H.C. and J.L. performed the experiments and simulations. H.C. and Y.W. analyzed the data and developed the theory. H.C. and Z.C. conducted the cell-related experiments. X.D. and K.F. completed the setup for the experiments. F.D. contributed to in vivo biosafety tests. H.C. and J.Y. completed the figures and wrote the manuscript. All the authors participated in discussions and revised the manuscript. Z.W., F.D., Y.S., and J.Y. supervised the project. **Competing interests:** The authors declare that they have no competing interests. **Data and materials availability:** All data needed to evaluate the conclusions in the paper are present in the paper and/or the Supplementary Materials.

Submitted 25 June 2024
Accepted 5 February 2025
Published 12 March 2025
10.1126/sciadv.adr3356